Rectification of evanescent heat transfer between dielectric-coated and uncoated silicon carbide plates

Hideo Iizuka and Shanhui Fan

Related Articles

Reduction of mean-square advection in turbulent passive scalar mixing
Phys. Fluids 24, 075104 (2012)

Scaling range of velocity and passive scalar spectra in grid turbulence
Phys. Fluids 24, 075101 (2012)

Nusselt number and friction factor correlations for solar air heater duct with broken V-down ribs combined with staggered rib roughness
J. Renewable Sustainable Energy 4, 033122 (2012)

Numerical study of the onset of thermosolutal convection in rotating spherical shells
Phys. Fluids 24, 064101 (2012)

When complexity leads to simplicity: Ocean surface mixing simplified by vertical convection
Phys. Fluids 24, 056603 (2012)

Additional information on J. Appl. Phys.

Journal Homepage: http://jap.aip.org/

Journal Information: http://jap.aip.org/about/about_the_journal

Top downloads: http://jap.aip.org/features/most_downloaded

Information for Authors: http://jap.aip.org/authors

Rectification of evanescent heat transfer between dielectric-coated and uncoated silicon carbide plates

Hideo Iizuka[1] and Shanhui Fan[2]

[1]*Toyota Central Research & Development Labs., Nagakute, Aichi 480 1192, Japan*
[2]*Department of Electrical Engineering, Stanford University, Stanford, California 94305, USA*

Here, we show analytically that the thermal rectification via evanescent waves is obtained in the parallel semi-infinite bodies of the dielectric-coated silicon carbide and uncoated silicon carbide. The permittivity and the thickness of the dielectric coating are derived for maximizing the thermal rectification. In the nonequilibrium situation holding temperatures of 500 K for one body and 300 K for the other, either a coating with a high permittivity of 14 and a thickness of 1 nm or a coating with a low permittivity of 2 and a thickness exceeding 10 nm, results in rectifying coefficients of 0.4 to 0.44. © *2012 American Institute of Physics.* [http://dx.doi.org/10.1063/1.4737465]

I. INTRODUCTION

In the near field regime, the electromagnetic heat transfer between a hot body and a cold body is enhanced by orders of magnitude compared to the far-field blackbody limit, due to the contributions from the evanescent waves of the bodies when the two bodies are sufficiently close to each other.[1–3] Such enhancement opens up the potential applications such as thermophotovoltaics,[4] thermal radiation scanning tunneling microscopy,[5] heat-assisted magnetic recording,[6] and nanolithography.[7]

Various geometries for the near-field heat transfer have been theoretically investigated, including two spherical bodies,[8] a sphere and a plate,[9,10] a sphere and a structured surface,[11,12] one-dimensional photonic crystals,[13] gratings,[14,15] porous slabs,[16] thin films,[17] and many bodies.[18] Near-field heat transfer behaviors of doped silicon,[19] meta-materials,[20,21] and between graphene and amorphous silica[22] have been also investigated. Experimental demonstrations of parallel plates[23,24] and sphere-plate structures[25–27] have verified that the evanescent heat transfer enhancement can exceed the blackbody limit.

A thermal rectification scheme via evanescent waves was presented in Ref. 28, where the rectification relied on the temperature dependence of electromagnetic resonances. The system consisted of one half-space of isotropic 3C polytype silicon carbide (SiC-3C) and the other half-space of uniaxial 6 H polytype silicon carbide (SiC-6H), separated by a vacuum gap. A film and a half-space of doped silicon with different doping levels also showed a thermal rectification characteristic.[29]

In this paper, we present a rectification system between the same material bodies. Our geometry consists of one half-space of SiC having the transparent dielectric coating, and the other half-space of SiC that has no coating. The same material structure extends the degrees of freedom for designs of thermal rectification devices. The coating permittivity and thickness are very important parameters for the thermal rectification performance. Our paper is organized as follows: In Sec. II, the configuration of the rectification system and the formalism of the near-field heat transfer are presented. The coating permittivity and thickness condition are derived for maximizing the rectification performance. In other studies on the near-field transfer, coated plates were investigated[30] and the maximum heat flux[31,32] was discussed. But these works[30–32] did not study rectification effects. In Sec. III, numerical results of the thermal rectification are presented. We also present the dispersion analysis that complements the direct fluctuational electrodynamic calculations presented in Sec. II. Such dispersion analysis provides additional insights into the thermal rectification effects. The concluding remarks are then given in Sec. IV.

II. THERMAL RECTIFICATION IN FOUR MEDIA STRUCTURE

A. Configuration

Figure 1 shows the configuration of a rectification system. It consists of the two semi-infinte SiC plates; the bottom semi-infinite SiC plate has the dielectric coating and the top semi-infinite SiC plate has no coating. The plates are separated by a vacuum gap. Electromagnetic resonances at the surfaces of SiC plates are temperature dependent.[28] The nonequilibrium situation is considered where the two plates maintain different temperatures T_H and T_L ($T_H > T_L$). The forward temperature-biased scenario is defined as the top plate held at temperature T_H and the bottom plate held at temperature T_L. While in the reverse temperature-biased scenario, the temperatures of T_H and T_L are swapped, i.e., the top plate and the bottom plate hold temperatures of T_L and T_H, respectively. Both the top and the bottom bodies support electromagnetic surface resonances at the vacuum interfaces. The one-sided dielectric coating on the bottom plate in Fig. 1 can manipulate the electromagnetic resonance at the surface of the bottom plate. As a result, the wavelength of the surface resonances of the two plates coincide in the forward biased scenario, while differ in the reverse biased scenario, resulting in thermal rectification effect.[28] To achieve maximum rectification, we consider, in this paper, the effects of both the permittivity and the thickness of the coating.
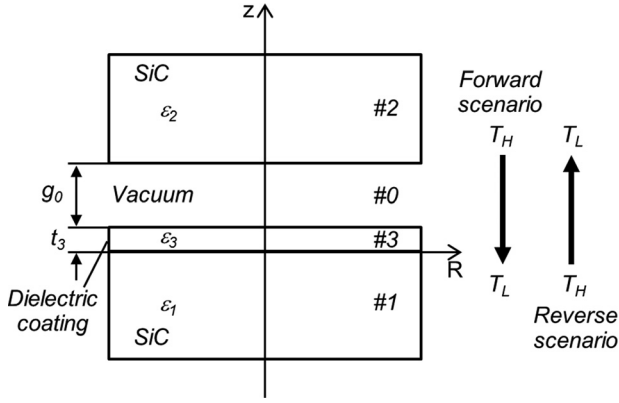
FIG. 1. Configuration of the thermal rectification system consisting of the dielectric-coated silicon carbide (SiC) plate and the uncoated SiC plate (dimensions: $g_0 + t_3 = 100$ nm, t_3 is variable, temperatures: $T_H = 500$ K and $T_L = 300$ K, permittivities: ε_1 and ε_2 are referred to Ref. 34. ε_3 is variable).

B. Formalism

In our formalism, the vacuum region, bottom SiC plate, top SiC plate, and dielectric coating are represented by media numbers 0, 1, 2, and 3, respectively. The cylindrical coordinate system (R, ϕ, z) is used in Fig. 1. It is assumed that the top and bottom plates are nonmagnetic, isotropic, and homogeneous and that the dielectric coating is transparent, i.e., $\varepsilon_3 = Re(\varepsilon_3)$. The heat transfer between the plates can be calculated from the fluctuational electrodynamics by determining the ensemble average of Poynting vector, represented as a cross correlation function of electric and magnetic fields.[1] The fields are obtained by integrating contributions from the thermal current sources whose strengths are provided by the fluctuation dissipation theorem and by using the dyadic Green's functions of the system.

We first consider the forward temperature-biased scenario. The transmittance from medium 1 with T_L to medium 2 with T_H in the four media of Fig. 1 is given by[33]

$$T_{12,j}(\omega, \beta, T_L, T_H)$$
$$= \frac{t_{13,j} t_{30,j} t_{02,j} e^{i\gamma_3 t_3 + i\gamma_0 g_0}}{1 - r_{31,j} r_{30,j} e^{2i\gamma_3 t_3} - r_{03,j} r_{02,j} e^{2i\gamma_0 g_0} - r_{31,j} r_{02,j} e^{2i\gamma_3 t_3 + 2i\gamma_0 g_0}},$$
$$(j = p, s), \tag{1}$$

where $t_{uv,j}$ and $r_{uv,j}$ are the Fresnel transmission and reflection coefficients from medium u to medium v for p-polarization

$(j = p)$ and s-polarization $(j = s)$. γ_u is the z-component of wavevector $\boldsymbol{k_u}$ in medium u and has the form $\gamma_u = \sqrt{\varepsilon_u k_0^2 - \beta^2}$, $(\beta \leq \sqrt{\varepsilon_u} k_0)$ for propagation waves and $\gamma_u = i\kappa_u = i\sqrt{\beta^2 - \varepsilon_u k_0^2}$, $(\sqrt{\varepsilon_u} k_0 \leq \beta)$ for evanescent waves. β, k_0, and ω are the *radial*-component of wavevector $\boldsymbol{k_u}$, the free space wavenumber, and the angular frequency, respectively. Note that Fresnel coefficients $t_{uv,j}$, $r_{uv,j}$, and the z-component of wavevector γ_u, $i\kappa_u$ are functions of ω and β for $u = 0, 3$ and are functions of ω, β, T_L, and T_H for $u = 1, 2$ due to the temperature-dependence of the permittivity. In the presentation that follows, the explicit dependence of various quantities on (ω, β), (ω, β, T_L), and (ω, β, T_H) are suppressed to avoid complicated expressions. The net ensemble average of the z-component of the cross correlation function of electric and magnetic fields at $z = g_0 + t_3$ is given by[19]

$$\langle \vec{S}_{12,z}(\omega, \beta, T_L, T_H) \rangle$$
$$= \Theta(\omega, T_L) \int_0^{+\infty} \frac{\beta d\beta}{4\pi^2} \left[|T_{12,s}(\omega, \beta, T_L, T_H)|^2 \frac{Re(\gamma_1) Re(\gamma_2)}{|\gamma_1|^2} \right.$$
$$\left. + |T_{12,p}(\omega, \beta, T_L, T_H)|^2 \frac{Re(\varepsilon_1 \gamma_1^*) Re(\varepsilon_2 \gamma_2^*)}{|\varepsilon_1||\varepsilon_2||\gamma_1|^2} \right], \tag{2}$$

where $\Theta(\omega, T) = \hbar\omega / \left(e^{\hbar\omega/(k_B T)} - 1 \right)$ is the mean thermal energy of a single optical mode at an angular frequency, $\hbar$ and k_B are the reduced Planck constant and the Boltzmann constant, respectively. Substituting Eq. (1) into Eq. (2), we obtain the net heat flux in the forward biased scenario

$$\phi_{Forward} = \int_0^{+\infty} d\omega [\langle \vec{S}_{21,z}(\omega, \beta, T_L, T_H) \rangle$$
$$- \langle \vec{S}_{12,z}(\omega, \beta, T_L, T_H) \rangle]$$
$$= \int_0^{+\infty} d\omega \{ [\Theta(\omega, T_H) - \Theta(\omega, T_L)]$$
$$\times \int_0^{+\infty} Z(\omega, \beta, T_L, T_H) \beta d\beta \}, \tag{3a}$$

where

$$\int_0^{+\infty} Z(\omega, \beta, T_L, T_H) \beta d\beta = \int_0^{k_0} \frac{\beta d\beta}{\pi^2} \left[\frac{\gamma_3 \gamma_0}{(\gamma_3 + \gamma_0)^2} (1 - |r_{31,s}|^2)(1 - |r_{02,s}|^2) \frac{1}{|D_{a,s}|^2} + \frac{\varepsilon_3 \gamma_3 \gamma_0}{(\gamma_3 + \varepsilon_3 \gamma_0)^2} (1 - |r_{31,p}|^2)(1 - |r_{02,p}|^2) \frac{1}{|D_{a,p}|^2} \right]$$
$$+ \int_{k_0}^{\sqrt{\varepsilon_3} k_0} \frac{2\beta d\beta}{\pi^2} \left[\frac{\gamma_3 \kappa_0}{\gamma_3^2 + \kappa_0^2} (1 - |r_{31,s}|^2) Im(r_{02,s}) \frac{e^{-2\kappa_0 g_0}}{|D_{b,s}|^2} + \frac{\varepsilon_3 \gamma_3 \kappa_0}{\gamma_3^2 + \varepsilon_3^2 \kappa_0^2} (1 - |r_{31,p}|^2) Im(r_{02,p}) \frac{e^{-2\kappa_0 g_0}}{|D_{b,p}|^2} \right]$$
$$+ \int_{\sqrt{\varepsilon_3} k_0}^{+\infty} \frac{4\beta d\beta}{\pi^2} \left[\frac{\kappa_3 \kappa_0}{(\kappa_3 + \kappa_0)^2} Im(r_{31,s}) Im(r_{02,s}) \frac{e^{-2\kappa_3 t_3 - 2\kappa_0 g_0}}{|D_{c,s}|^2} + \frac{\varepsilon_3 \kappa_3 \kappa_0}{(\kappa_3 + \varepsilon_3 \kappa_0)^2} Im(r_{31,p}) Im(r_{02,p}) \frac{e^{-2\kappa_3 t_3 - 2\kappa_0 g_0}}{|D_{c,p}|^2} \right], \tag{3b}$$

$$D_{a,j} = 1 - r_{31,j}r_{30,j}e^{2i\gamma_3 t_3} - r_{03,j}r_{02,j}e^{2i\gamma_0 g_0}$$
$$- r_{31,j}r_{02,j}e^{2i\gamma_3 t_3 + 2i\gamma_0 g_0}, \tag{3c}$$

$$D_{b,j} = 1 - r_{31,j}r_{30,j}e^{2i\gamma_3 t_3} - r_{03,j}r_{02,j}e^{-2\kappa_0 g_0}$$
$$- r_{31,j}r_{02,j}e^{2i\gamma_3 t_3 - 2\kappa_0 g_0}, \tag{3d}$$

$$D_{c,j} = 1 - r_{31,j}r_{30,j}e^{-2\kappa_3 t_3} - r_{03,j}r_{02,j}e^{-2\kappa_0 g_0}$$
$$- r_{31,j}r_{02,j}e^{-2\kappa_3 t_3 - 2\kappa_0 g_0}. \tag{3e}$$

$Z(\omega, \beta, T_L, T_H)$ is the exchange function introduced in Ref. 19 that characterizes the exchange behavior of electromagnetic waves between the plates at a single point of ω and β. Equation (3b) includes the contributions of both propagation and evanescent waves, i.e., propagation waves in the vacuum and coating regions for the first term ($0 < \beta \le k_0$), evanescent waves in the vacuum and propagation waves in the coating for the second term ($k_0 \le \beta \le \sqrt{\varepsilon_3}k_0$), and evanescent waves in the vacuum and coating for the third term ($\sqrt{\varepsilon_3}k_0 \le \beta$).

Similar to the forward biased scenario, the reverse biased scenario is characterized by swapping T_L and T_H in Eq. (3).

$$\phi_{Reverse} = \int_0^{+\infty} d\omega [\langle \vec{S}_{12,z}(\omega, \beta, T_H, T_L) \rangle$$
$$- \langle \vec{S}_{21,z}(\omega, \beta, T_H, T_L) \rangle]$$
$$= \int_0^{+\infty} d\omega \Big\{ [\Theta(\omega, T_H) - \Theta(\omega, T_L)]$$
$$\times \int_0^{+\infty} Z(\omega, \beta, T_H, T_L)\beta d\beta \Big\}. \tag{4}$$

The rectifying coefficient is defined as

$$R_{FR} = \frac{\phi_{Forward} - \phi_{Reverse}}{\phi_{Reverse}}. \tag{5}$$

Next, let us consider maximizing the integrand $Z(\omega, \beta, T_L, T_H)$ of the net heat flux in the forward biased scenario. In the extreme near-field regime investigated in this paper, i.e., the heat transfer occurs in $k_0 \ll \beta$, the evanescent p-polarization is dominant and $\beta \approx k_0 \approx k_3 \approx k_m$ is assumed. The integrand $Z(\omega, \beta, T_L, T_H)$ in Eq. (3b) can then be approximated with

$$Z(\omega_m, \kappa_m, T_L, T_H) \approx \frac{4}{\pi^2} \frac{\varepsilon_3}{(1 + \varepsilon_3)^2} Im(r_{31,p})Im(r_{02,p})$$
$$\times \frac{e^{-2\kappa_m(t_3 + g_0)}}{[Re(D_{c,p})]^2 + [Im(D_{c,p})]^2}, \tag{6a}$$

where

$$Re(D_{c,p}) = 1 - Re(r_{31,p})r_{30,p}e^{-2\kappa_m t_3} - r_{03,p}Re(r_{02,p})e^{-2\kappa_m g_0}$$
$$- Re(r_{31,p}r_{02,p})e^{-2\kappa_m(t_3 + g_0)}, \tag{6b}$$

$$Im(D_{c,p}) = -Im(r_{31,p})r_{30,p}e^{-2\kappa_m t_3} - r_{03,p}Im(r_{02,p})e^{-2\kappa_m g_0}$$
$$- Im(r_{31,p}r_{02,p})e^{-2\kappa_m(t_3 + g_0)}, \tag{6c}$$

$$r_{31,p} \approx \frac{\varepsilon_1 - \varepsilon_3}{\varepsilon_1 + \varepsilon_3}, \tag{6d}$$

$$r_{30,p} = -r_{03,p} \approx \frac{1 - \varepsilon_3}{1 + \varepsilon_3}, \tag{6e}$$

$$r_{02,p} \approx \frac{\varepsilon_2 - 1}{\varepsilon_2 + 1}. \tag{6f}$$

ω_m and κ_m are the angular frequency and the wavenumber when the integrand Z is maximal. To determine the optimal thickness, we use

$$\frac{\partial Z(\omega_m, \kappa_m, T_L, T_H)}{\partial t_3} = 0. \tag{7}$$

The third and the fourth terms in Eq. (6b) and the first to the third terms in Eq. (6c) are much smaller than the second term in Eq. (6b), $Re(r_{31,p})r_{30,p}e^{-2\kappa_m t_3}$. Then, Eq. (7) yields the simplified equation.

$$1 - Re(r_{31,p})r_{30,p}e^{-2\kappa_m t_3} \approx 0. \tag{8}$$

The coating thickness is given by

$$t_3 \approx \frac{1}{2k_m}ln[Re(r_{31,p})r_{30,p}] \approx \frac{1}{2k_m}ln\left[\frac{(|\varepsilon_1|^2 - \varepsilon_3^2)(1 - \varepsilon_3)}{|\varepsilon_1 + \varepsilon_3|^2(1 + \varepsilon_3)}\right]. \tag{9}$$

An interesting point here is that the optimal coating thickness is determined by the coating permittivity. Also, Eq. (9) indicates that the coating thickness for maximizing the integrand Z may be temperature dependence, due to the temperature dependence of ε_1. With regard to the maximum heat flux satisfying Eq. (9), it may not change so much with variation of t_3 when the distance, $g_0 + t_3$, between the SiC plates is kept constant. This can be understood by the fact that the heat flux between the plates is mainly determined by the distance when the top and bottom plates have the same electromagnetic resonance. It should be also mentioned that maximizing the integrand Z of the net heat flux in the forward biased scenario provides a good approximation for maximizing the thermal rectification. Because in the reverse biased scenario, electromagnetic resonances of the top and bottom plates are different with any parameters, and thus the heat flux in the reverse biased scenario is less sensitive to geometrical parameters.

III. RESULTS

The evanescent p-polarization is mainly discussed for the thermal rectification since it is the dominant polarization due to the fact that the surface resonance is p-polarized. The temperature dependence of the SiC permittivity is referred to Ref. 34 in the calculation. Temperatures are set at $T_H = 500\,\text{K}$ and $T_L = 300\,\text{K}$ for the top plate and the bottom plate in the forward biased scenario and for the bottom plate and the top plate in the reverse biased scenario, respectively. A distance of $g_0 + t_3 = 100\,\text{nm}$ between the SiC plates is kept constant when the coating thickness t_3 is varied. Figures 2(a) and 2(b) show the net spectral heat fluxes of the p-polarized evanescent wave with the two coating parameter sets that meet Eq. (9); (a) $\varepsilon_3 = 2$, $t_3 = 10\,\text{nm}$ and (b) $\varepsilon_3 = 14$, $t_3 = 1\,\text{nm}$. A
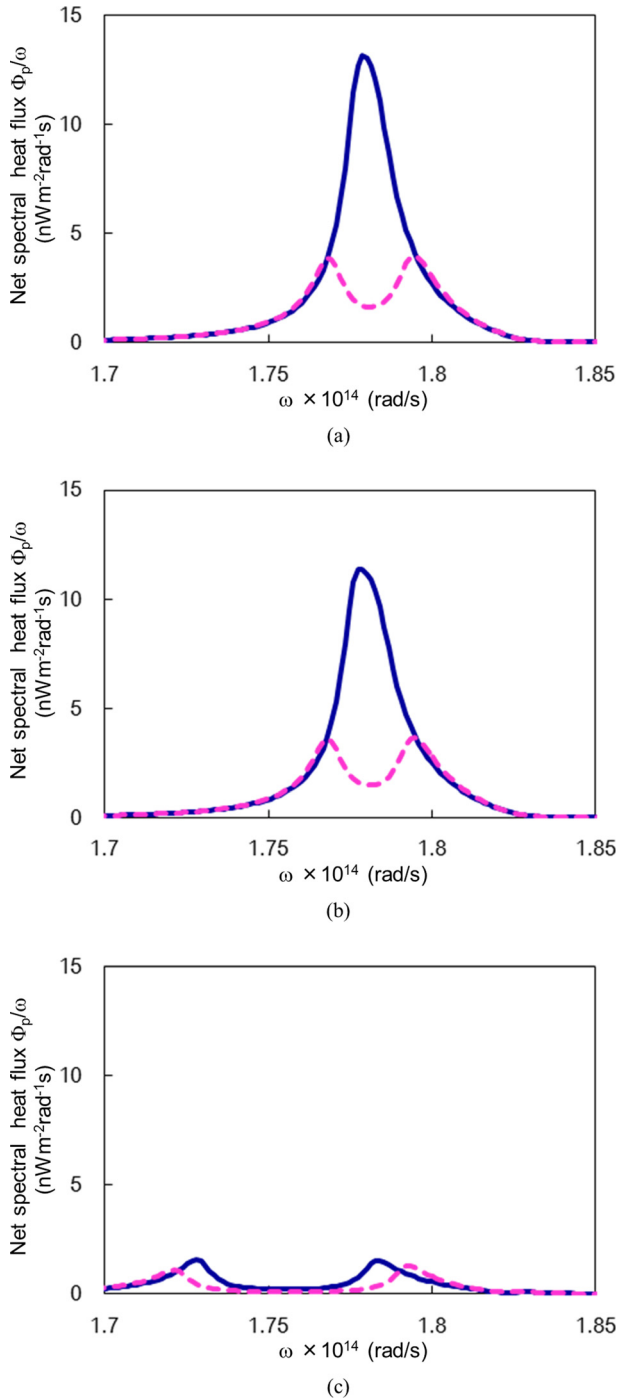
FIG. 2. Net spectral heat fluxes of the p-polarized evanescent wave for the forward and reverse temperature-biased scenarios. (a) $\varepsilon_3 = 2$, $t_3 = 10$ nm, (b) $\varepsilon_3 = 14$, $t_3 = 1$ nm, (c) $\varepsilon_3 = 14$, $t_3 = 10$ nm. (a) and (b) meet Eq. (9), while (c) does not meet it (solid lines: forward biased scenario, dashed lines: reverse biased scenario).

spectral peak is observed at $\omega = 1.78 \times 10^{14}$ rad/s in the forward biased scenario (solid line) and it is suppressed in the reverse biased scenario (dashed line) in both parameter sets. On the other hand, no peak is observed in Fig. 2(c), where parameters of (c) $\varepsilon_3 = 14$, $t_3 = 10$ nm do not meet Eq. (9). This is due to the fact that the electromagnetic resonance of the bottom plate is shifted down to $\omega = 1.73 \times 10^{14}$ rad/s.

The coating condition is next numerically investigated. The net heat flux is calculated with variation of ε_3 from 2 to

15 with a step of 1 nm and t_3 from 1 nm to 15 nm with a step of 1 nm. The total number of structures considered is 210. The coating permittivity and thickness are plotted in the ε_3-t_3 diagram of Fig. 3(a) when the rectifying coefficients are larger than 0.4. Here, we include the contributions of both polarizations, as well as contributions from both propagating and evanescent fields. The result of Eq. (9), represented by the solid line, agrees with the plots in Fig. 3(a). In applying Eq. (9), we used $k_m = 41k_0$, which is obtained by the dispersion analysis as shown in Fig. 5(a) and discussed in details later. The validity of the coating condition was confirmed. It should be mentioned that the rectifying coefficient larger than 0.4 is obtained with variation of the coating thickness t_3 from 1 nm to 15 nm when the coating permittivity ε_3 is properly selected to meet the coating condition of Eq. (9). We also compare the rectification coefficients that include contributions from all-components with the contribution only from the p-polarized evanescent wave [Fig. 3(b)]. Including only the contribution from the p-polarized evanescent wave, the rectifying coefficient ranges from 0.6 to 0.67. Since other components such as the s-polarized evanescent wave,
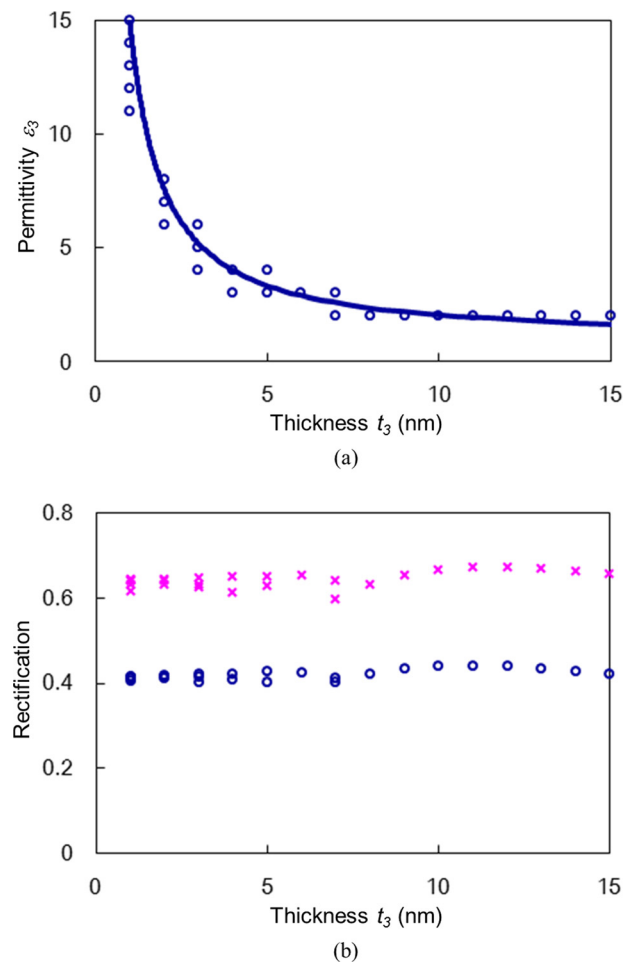

FIG. 3. (a) Relationship of the coating permittivity and thickness and (b) rectifying coefficients that are plotted when the rectifying coefficients are larger than 0.4. The solid curve is the result of Eq. (9) derived for maximizing the rectification, and circles are the results of the heat flux calculation in (a). Crosses and circles represent the evanescent p-polarization contribution and all-components contributions; p- and s-polarized evanescent and propagation waves, respectively, in (b).

p-polarized, and s-polarized propagation waves are not changed in the forward and reverse biased scenarios, the rectifying coefficients by all-components contributions are values of 0.4 to 0.44. This finding about the coating permittivity and thickness condition, particularly, low permittivity with increasing the coating thickness, may be useful when the accuracy of nanofabrication technology is considered for designs of thermal rectification devices.

Figure 4 shows vacuum gap dependence characteristics of rectifying coefficients with the coating permittivity and thickness fixed. The rectifying coefficients are less sensitive to the gap variation with narrow gaps, e.g., $g_0 \leq 100$ nm for the contribution only from the p-polarized evanescent wave (dashed line) and $g_0 \leq 50$ nm for all-components contributions (solid line). The rectifying coefficients go down with wider gaps, indicating that the rectifying effect here is a near-field effect.[28] Also the comparison of the two curves shows up that the rectifying coefficient by all-components contributions (solid line) becomes close to the rectifying coefficient including the contribution from the p-polarized evanescent wave (dashed line) with narrower gaps since the p-polarized evanescent wave becomes dominant in the heat flux. These come from the nature of the evanescent wave based thermal rectification scheme.[28]

The evanescent heat transfer behavior of the four media structure is further investigated with coating parameters of $\varepsilon_3 = 2$, $t_3 = 10$ nm [Fig. 2(a)]. Figures 5(a) and 5(b) show the integrand Z distributions of the p-polarized evanescent wave in the ω-β diagram for the forward and reverse biased scenarios that are normalized by each maximum value. It is observed in Fig. 5(a) that the strong heat transfer occurs in $k_0 \ll \beta$; the normalized value of the integrand Z is higher than 0.5 in the range of β from $32k_0$ to $59k_0$ at $\omega = 1.78 \times 10^{14}$ rad/s in the forward biased scenario. On the other hand, the integrand Z is suppressed at this angular frequency in the reverse biased scenario as shown in Fig. 5(b).

The behavior of the integrand, as shown in Fig. 5, can be understood by analyzing the dispersion relation of the layered structure here. Following to multilayers dispersion

FIG. 5. Normalized integrand Z distributions (black-red-white colorscale) of Eq. (3b) for the p-polarized evanescent wave in the ω-β plane when the coating has parameters of $\varepsilon_3 = 2$ and $t_3 = 10$ nm [Fig. 2(a)]. Dispersion curves (green lines) of Eq. (10) are also plotted. (a) Forward biased scenario and (b) reverse biased scenario.
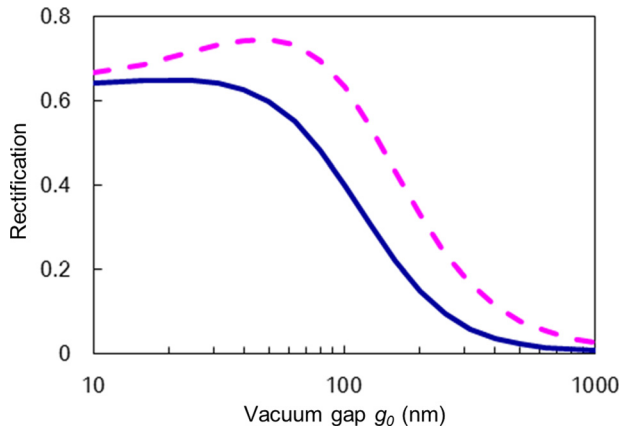

FIG. 4. Vacuum gap dependence characteristics of rectifying coefficients when the coating parameters are fixed with $\varepsilon_3 = 2$ and $t_3 = 10$ nm [Fig. 2(a)]. The solid curve includes all-components contributions; p- and s-polarized evanescent and propagation waves, while the dashed line includes only the p-polarized evanescent wave contribution.
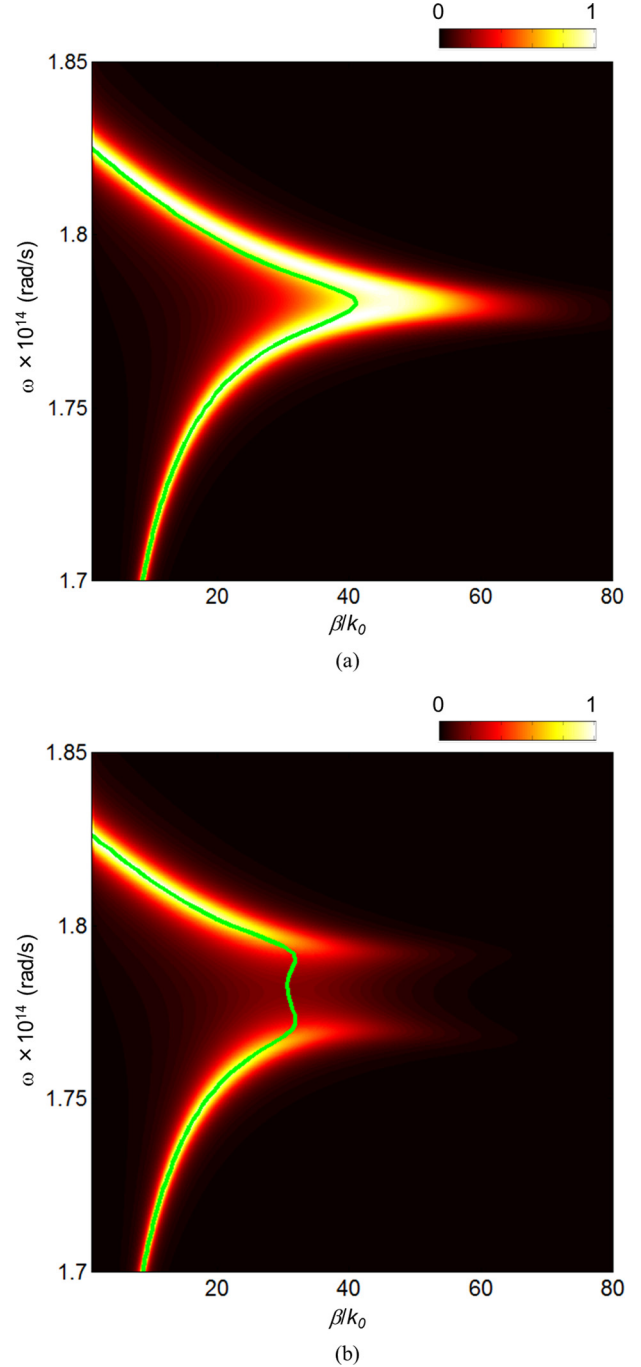
investigations given in Ref. 35, the dispersion equation for the four media structure of Fig. 1 is given by

$$\left[\left(\frac{\varepsilon_2}{\kappa_2} - \frac{\varepsilon_0}{\kappa_0} \right) \left(\frac{\varepsilon_0}{\kappa_0} + \frac{\varepsilon_3}{\kappa_3} \right) e^{-\kappa_0 g_0} + \left(\frac{\varepsilon_2}{\kappa_2} + \frac{\varepsilon_0}{\kappa_0} \right) \left(\frac{\varepsilon_0}{\kappa_0} - \frac{\varepsilon_3}{\kappa_3} \right) e^{\kappa_0 g_0} \right]$$

$$\times \left(\frac{\varepsilon_3}{\kappa_3} - \frac{\varepsilon_1}{\kappa_1} \right) e^{-\kappa_3 t_3} + \left[\left(\frac{\varepsilon_2}{\kappa_2} - \frac{\varepsilon_0}{\kappa_0} \right) \left(\frac{\varepsilon_0}{\kappa_0} - \frac{\varepsilon_3}{\kappa_3} \right) e^{-\kappa_0 g_0} \right.$$

$$\left. + \left(\frac{\varepsilon_2}{\kappa_2} + \frac{\varepsilon_0}{\kappa_0} \right) \left(\frac{\varepsilon_0}{\kappa_0} + \frac{\varepsilon_3}{\kappa_3} \right) e^{\kappa_0 g_0} \right] \left(\frac{\varepsilon_3}{\kappa_3} + \frac{\varepsilon_1}{\kappa_1} \right) e^{\kappa_3 t_3} = 0. \quad (10)$$

Dispersion curves are also plotted in Figs. 5(a) and 5(b) for the forward and reverse biased scenarios. The dispersion curves describe the fluctuational electrodynamics results well, comparing to the integrand Z distributions; β has a peak of $41k_0$ at $\omega = 1.78 \times 10^{14}$ rad/s in the forward biased scenario. This peak value was used for the calculation of Eq. (9) with $k_m = 41k_0$ as mentioned. While in the reverse biased scenario, β has two peaks at $\omega = (1.78 \pm 0.01) \times 10^{14}$ rad/s.

Temperatures have so far been fixed with $T_H = 500$ K and $T_L = 300$ K. Here, the temperature dependence of the thermal rectification performance is investigated with variation of T_H from 300 K to 700 K, holding $T_L = 300$ K. The coating permittivity is set at $\varepsilon_3 = 2$. The maximum achievable rectifying coefficient (solid line) is plotted in Fig. 6(a) when the coating thickness t_3 is selected (solid line) as shown in Fig. 6(b). The thermal rectification includes all-components contributions of p- and s-polarized evanescent and propagation waves. The maximum achievable rectification increases with increasing the temperature difference
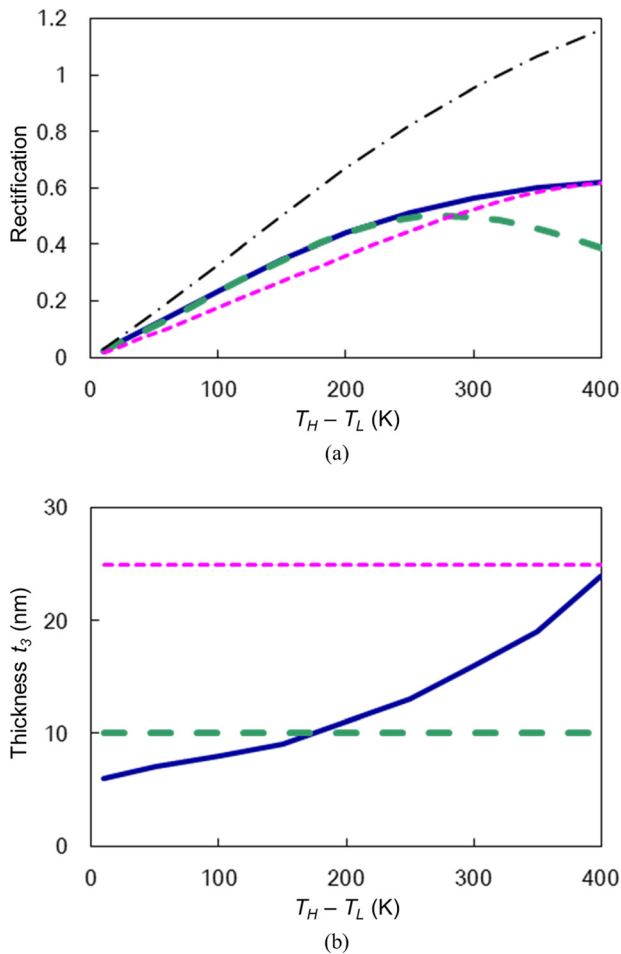
$T_H - T_L$, since the split in the frequency of the electromagnetic surface resonance between T_H and T_L becomes larger. The optimum coating becomes thicker with the increase in the temperature difference [Fig. 6(b)] since at larger temperature difference the split of the surface resonance frequencies becomes larger, and needs to be compensated with a thicker layer in order to achieve resonance overlap in the forward biased scenario. The temperature dependence characteristics with $t_3 = 10$ nm (dashed line) and 25 nm (dotted line) are also presented in Fig. 6(a); $t_3 = 10$ nm provides the maximum achievable rectification with $T_H - T_L$ up to 250 K, and the further increase in T_H makes the rectifying coefficient decrease. While $t_3 = 25$ nm provides the maximum achievable rectification at $T_H - T_L = 400$ K and the lower values as T_H decreases. This investigation result reveals that the maximum rectification can be obtained with a proper choice of the coating thickness t_3 depending on temperatures of T_H and T_L. The thermal rectification system of Fig. 1 would work effectively, when temperatures of dominant operations are taken into account for designs. With regard to the evanescent p-polarization only considered, the maximum achievable rectifying coefficient increases with the increase of T_H, and reaches 1.16 at $T_H - T_L = 400$ K.

The transparent dielectric coating is assumed throughout the paper. Materials that have a permittivity of around two and are transparent around the peak angular frequency $\omega = 1.78 \times 10^{14}$ rad/s include barium fluoride and strontium fluoride.[36] The coating material loss at frequency ranges far away from that peak angular frequency may not affect the rectification performance that is mainly characterized by the resonance peak of the p-polarized evanescent wave. Also, the thermal expansion of the coating material and SiC should be taken into account in practical designs.

FIG. 6. (a) Maximum achievable thermal rectifying coefficients (solid line) with variation of the high temperature T_H, holding $T_L = 300$ K when (b) the coating thickness t_3 is adjusted (solid line) with $\varepsilon_3 = 2$. The temperature dependence characteristics of rectifying coefficients with $t_3 = 10$ nm (dashed line) and 25 nm (dotted line) are also presented. The three curves (solid, dashed, and dotted lines) include all-components contributions; p- and s-polarized evanescent and propagation waves, while the dashed-dotted line includes only the p-polarized evanescent wave contribution in (a).

IV. CONCLUSIONS

In the parallel semi-infinite bodies of dielectric-coated SiC and uncoated SiC, the dielectric permittivity and thickness condition were derived for maximizing the thermal rectification. The fluctuational electrodynamics calculation results including all-components contributions of p- and s-polarized evanescent and propagation waves showed rectifying coefficients of 0.4 to 0.44 in a temperature set of 500 K and 300 K, when the coating condition was met. High permittivity coatings, e.g., $\varepsilon_3 = 14$, needed a thin thickness of $t_3 = 1$ nm, while low permittivity coatings, e.g., $\varepsilon_3 = 2$, increased the thickness by $t_3 = 10$ nm and more that would allow us to fabricate devices.

[1] D. Polder and M. Van Hove, Phys. Rev. B **4**, 3303 (1971).
[2] J. J. Loomis and H. J. Maris, Phys. Rev. B **24**, 18517 (1994).
[3] J. B. Pendry, J. Phys.: Condens. Matter **11**, 6621 (1999).

[4]M. Francoeur, R. Vaillon, and M. P. Menguc, IEEE Trans. Energy Convers. **26**, 686 (2011).

[5]Y. D. Wilde, F. Formanek, R. Carminati, B. Gralak, P.-A. Lemoine, K. Joulain, J.-P. Mulet, Y. Chen, and J.-J. Greffet, Nature **444**, 740 (2006).

[6]W. A. Challener, C. Peng, A. V. Itagi, D. Karns, W. Peng, Y. Peng, X. M. Yang, X. Zhu, N. J. Gokemeijer, Y.-T. Hsia, G. Ju, R. E. Rottmayer, M. A. Seigler, and E. C. Gage, Nature Photon. **3**, 220 (2009).

[7]L. Wang, S. M. Uppuluri, E. X. Jin, and X. Xu, Nano Lett. **6**, 361 (2006).

[8]A. I. Volokitin and B. N. J. Persson, Phys. Rev. B **63**, 205404 (2001).

[9]C. Otey and S. Fan, Phys. Rev. B **84**, 245431 (2011).

[10]M. Kruger, T. Emig, and M. Kardar, Phys. Rev. Lett. **106**, 210404 (2011).

[11]S.-A. Biehs, O. Huth, and F. Ruting, Phys. Rev. B **78**, 085414 (2008).

[12]S.-A. Biehs and J.-J. Greffet, Phys. Rev. B **81**, 245414 (2010).

[13]P. Ben-Abdallah, K. Joulain, and A. Pryamikov, Appl. Phys. Lett. **96**, 143117 (2010).

[14]A. W. Rodriguez, O. Ilic, P. Bermel, I. Celanovic, J. D. Joannopoulos, M. solijacic, and S. G. Johnson, Phys. Rev. Lett. **107**, 114302 (2011).

[15]S.-A. Biehs, F. S. S. Rosa, and P. Ben-Abdallah, Appl. Phys. Lett. **98**, 243102 (2011).

[16]S.-A. Biehs, P. Ben-Abdallah, F. S. S. Rosa, K. Joulain, and J.-J. Greffet, Opt. Express **19**, A1088 (2011).

[17]M. Francoeur, M. P. Menguc, and R. Vaillon, Phys. Rev. B **84**, 075436 (2011).

[18]P. Ben-Abdallah and S.-A. Biehs, Phys. Rev. Lett. **107**, 114301 (2011).

[19]C. J. Fu and Z. M. Zhang, Int. J. Heat Mass Transfer **49**, 1703 (2006).

[20]K. Joulain and J. Drevillon, Phys. Rev. B **81**, 165119 (2010).

[21]M. Francoeur, S. Basu, and S. J. Petersen, Opt. Express **19**, 18774 (2011).

[22]A. I. Volokitin and N. J. Persson, Phys. Rev. B **83**, 241407 (2011).

[23]L. Hu, A. Narayanaswamy, X. Chen, and G. Chen, Appl. Phys. Lett. **92**, 133106 (2008).

[24]R. S. Ottens, V. Questschke, S. Wise, A. A. Alemi, R. Lundock, G. Mueller, D. H. Reitze, D. B. Tanner, and B. F. Whiting, Phys. Rev. Lett. **107**, 014301 (2011).

[25]A. Narayanaswamy, S. Shen, and G. Chen, Phys. Rev. B **78**, 115303 (2008).

[26]S. Shen, A. Narayanaswamy, and G. Chen, Nano Lett. **9**, 2909–2913 (2009).

[27]E. Rousseau, A. Siria, G. Jourdan, S. Volz, F. Comin, J. Chevrier, and J.-J. Greffet, Nature Photon. **3**, 514 (2009).

[28]C. R. Otey, W. T. Lau, and S. Fan, Phys. Rev. Lett. **104**, 154301 (2010).

[29]S. Basu and M. Francoeur, Appl. Phys. Lett. **98**, 113106 (2011).

[30]S. Basu, Z. M. Zhang, and C. J. Fu, Int. J. Energy Res. **33**, 1203–1232 (2009).

[31]S. Basu and Z. M. Zhang, J. Appl. Phys. **105**, 093535 (2009).

[32]S. Basu and M. Francoeur, Appl. Phys. Lett. **98**, 243120 (2011).

[33]W. C. Chew, *Waves and Fields in Inhomogeneous Media* (IEEE, New York, 1995).

[34]D. Olego and M. Cardona, Phys. Rev. B **25**, 3889 (1982).

[35]E. N. Economou, Phys. Rev. **182**, 539 (1969).

[36]E. D. Palik, *Handbook of Optical Constants of Solids* (Academic, New York, 1985).